

# MONITORING THE SMALL DEBRIS ENVIRONMENT WITH GROUND-BASED RADAR: AN ASSESSMENT OF DATA FROM 2016-2023

Alyssa Manis<sup>(1)</sup>, Jessica Arnold Headstream<sup>(1)</sup>, Michael Poehlmann<sup>(2)</sup>, Phillip Anz-Meador<sup>(3)</sup>,  
and Mark Matney<sup>(1)</sup>

<sup>(1)</sup> NASA Orbital Debris Program Office, NASA Johnson Space Center, Mail Code XI5-9E,  
2101 NASA Parkway, Houston, TX 77058, USA

<sup>(2)</sup> Intuitive Machines, Amentum JETS II Contract, NASA Johnson Space Center, Mail Code JS24,  
Houston, TX 77058, USA

<sup>(3)</sup> Amentum Services, Inc., NASA Johnson Space Center, Mail Code JS24, Houston, TX 77058, USA

## ABSTRACT

The NASA Orbital Debris Program Office (ODPO) has led efforts to characterize the small orbital debris (OD) environment using ground-based radar observations since the early 1990s. Measurements are collected using specialized sensors capable of statistically sampling objects too small to be tracked by the U.S. Space Surveillance Network (SSN), yet may pose the greatest threat to human spaceflight and robotic missions. The Haystack Ultrawideband Satellite Imaging Radar (HUSIR) – formerly Haystack – operated by the Massachusetts Institute of Technology Lincoln Laboratory (MIT/LL) has historically provided data on debris with sizes down to approximately 5 mm at 1000 km altitude and 2-3 cm throughout low Earth orbit (LEO). The Goldstone Orbital Debris Radar (Goldstone), operated by NASA’s Jet Propulsion Laboratory (JPL), has provided data on OD as small as approximately 2-3 mm for altitudes below 1000 km, some of the most sensitive ground-based measurements achievable at these altitudes. Together, HUSIR and Goldstone nominally provide over 500 hours of data each year, on average. The long record of regular measurements from these radars provides a unique opportunity to assess the trends over time of both the overall environment and individual debris-generating events. This paper provides a summary of HUSIR and Goldstone observations of debris below the size threshold of the SSN and their temporal evolution from 2016 through 2023. Specific debris-generating events are analyzed further, including the debris clouds from major collisions and explosions, the special sodium-potassium (NaK) population at approximately 65° inclination, and a persistent debris cloud evident at approximately 82° inclination.

## 1 INTRODUCTION

The NASA Orbital Debris Program Office (ODPO) primarily uses ground-based radars to provide data on

orbital debris (OD) in low Earth orbit (LEO). These sensors are operated in a specialized manner to enable statistical sampling of the OD environment from a few millimeters in size up to the limit of the public U.S. Space Surveillance Network (SSN) catalog at approximately 10 cm. This data is used to develop, verify, and validate models of the OD environment, in particular the NASA Orbital Debris Engineering Model (ORDEM). ORDEM is used primarily by satellite designers and operators to compute the mission risk to their vehicles from OD impacts. Consistent radar measurements are essential to capture the dynamic behavior of the OD environment and support regular and timely model updates.

Since 1990, the ODPO has partnered with the U.S. Department of Defense and the Massachusetts Institute of Technology Lincoln Laboratory (MIT/LL) to collect data using the Haystack Ultrawideband Satellite Imaging Radar (HUSIR) located in Westford, Massachusetts. Originally named Haystack, this radar was renamed after significant upgrades were completed from 2010 to 2013; data collected by the radar before and after the upgrade will be referred to herein by their respective name. Until early 2020, the ODPO also received data from the Haystack Auxiliary Radar (HAX), also operated by the MIT/LL, which provided continuity of statistical coverage between HUSIR and the SSN. Subsequently, preference of operating time was given to the more sensitive HUSIR as the addition of the Space Fence decreased the limiting size of the SSN catalog to smaller sizes historically covered by HAX. In addition, the Goldstone Orbital Debris Radar (Goldstone), part of the Deep Space Communications Complex near Barstow, California, and operated by the NASA Jet Propulsion Laboratory (JPL), has contributed data to the ODPO since 1993. HUSIR is the primary radar used by the ODPO to collect measurements on OD below the approximate SSN size threshold and provides coverage of debris with nominal sizes down to a completeness limit of approximately 5 mm at altitudes less than 1000 km and 2-3 cm throughout

LEO. Goldstone can detect smaller debris than HUSIR, providing data on OD down to a completeness size of approximately 2 mm at altitudes less than 1000 km. The two independent but complementary sensors provide a means to cross-validate results as well as cover a wider range of sizes than would be possible with a single sensor.

Given the long record of consistent debris observations from HUSIR and Goldstone, the ODPO is able to monitor the overall trends in the OD environment as well as both short- and long-term effects from individual breakups and other debris-generating events. This paper gives an overview of HUSIR and Goldstone operations, provides a snapshot of millimeter- and centimeter-sized OD as of 2023, and compares the evolution of these populations as seen by these sensors. Due to upgrades made to the software used by the ODPO to process data from HUSIR, only data processed using the same version of the software is considered here to ensure a consistent comparison of data through the years. Thus, data obtained from HUSIR and Goldstone from 2016 through 2023 are discussed. Some special data collects for specific major breakup events prior to 2016 are included as a reference for environment changes. In addition, the background, evolution, and current status of several major debris-generating events are discussed. These include the major collisions of the *Fengyun 1C* (FY-1C) anti-satellite (ASAT) test, the accidental collision of Iridium 33 (I33) and Cosmos 2251 (C2251), and the Cosmos 1408 (C1408) ASAT test, as well as explosions of the NOAA-16 spacecraft and a Long March 6A (CZ-6A) upper stage. The temporal behavior of other special populations, including the sodium-potassium (NaK) droplets and a so-called “82° cloud” evident at approximately 82° inclination, is also analyzed.

## 2 RADAR SYSTEM OVERVIEW

For OD observations, HUSIR and Goldstone operate in a beampark or staring mode, fixed at selected elevation and azimuth angles, and detect debris that pass through the radar beam. In this way, they are able to statistically sample the population of small OD down to a limiting size that is smaller than the limit possible for sensors operating in a typical tracking mode. HUSIR is a monostatic radar that uses a single 36.6 m-diameter antenna to transmit and receive. Goldstone is a bistatic system that uses 70 m and 34 m diameter dishes for the transmit and receive antennas, respectively. HUSIR and Goldstone both operate at X-band and transmit right-hand circularly polarized waveforms, receiving both right- and left-hand circularly polarized returns, referred to as the orthogonal polarization (OP) and principal polarization (PP),

respectively. HUSIR transmits a pulsed continuous wave (CW) waveform. Historically, the waveform had a center frequency of 10 GHz. This was modified to 10.1 GHz starting in 2020 to mitigate radio frequency interference [1, 2], and 10.1 GHz has been used exclusively since 1 October 2021. Goldstone transmits a pulsed linear frequency modulated “chirp” waveform centered at 8.56 GHz. A summary of the current nominal operating parameters for HUSIR and Goldstone is given in Tab. 1; here, sensitivity is defined as the single pulse signal-to-noise ratio (SNR) for an object with a radar cross section (RCS) of one square meter at 1000 km slant range.

*Table 1. HUSIR and Goldstone nominal operating parameters.*

| Operating Parameter                    | HUSIR  | Goldstone                         |
|--|--------|-----------------------------------|
| Peak Transmit Power (kW)               | 250    | 440                               |
| Transmit Frequency (GHz)               | 10.1   | 8.56                              |
| Wavelength (cm)                        | 3.0    | 3.5                               |
| Antenna Diameter (m)                   | 36.6   | 70 (Transmit)<br>34 (Receive)     |
| Half-power Beamwidth (deg)             | 0.058  | 0.03 (Transmit)<br>0.06 (Receive) |
| Sensitivity (dB)                       | 59.2   | 67.7                              |
| Intermediate Frequency Bandwidth (MHz) | 1.25   | 1.5                               |
| Pulse (chirp) Duration (ms)            | 1.6384 | 2.9                               |
| Pulse (chirp) Bandwidth (kHz)          | N/A    | 300                               |
| Pulse Repetition Frequency (Hz)        | 60     | 55.6                              |

Typical HUSIR pointing geometries are 75° elevation, due east (75E); 20° elevation, due south (20S); and 10° elevation, due south (10S). Approximately two-thirds of the HUSIR data are collected using the 75E pointing. By staring just off-zenith, the 75E staring geometry allows the radar to measure Doppler shifts that give meaningful orbital information for orbital inclinations between approximately 40° and 140° using a circular orbit approximation. With the 75E staring geometry, HUSIR samples between 392 km and 2166 km altitude. All HUSIR data presented here are from the 75E pointing.

Goldstone uses the Deep Space Station (DSS)-14 antenna as a transmitter pointed at 75E, with the receiver pointed so that the transmit and receive beams intersect across an altitude region of interest. DSS-15 was used as a receiver until its decommissioning in early 2018. The DSS-14/DSS-15 configuration provided a relatively short baseline of 500 m between transmitter and receiver, which allowed coverage of LEO with a single pointing. Since 2020, DSS-25 and DSS-26 of the Deep Space Network Apollo Cluster have been used as receivers, increasing the baseline to 10 km. This large baseline causes the antenna beams to overlap for a small part of LEO for a given pointing, so a new observation strategy was developed to optimize coverage over specific altitudes of interest [3]. During 2018, while a new observation strategy was being developed, a targeted 800 km range was used for OD detections, providing coverage over a limited altitude range of approximately 700 km to 850 km. From 2020 through 2023, the ODPO used four pointings termed “A,” “B,” “C,” and “D” to provide coverage of altitudes between 700 km to 1000 km without significant sensitivity loss relative to the historical configuration. Tab. 2 compares the minimum and maximum altitude coverage of HUSIR, the legacy Goldstone configuration (assuming the 3 dB beam overlap), the 2018 pointing targeted at 800 km range, and the new Goldstone pointings A-D.

Table 2. Altitude coverage of HUSIR, Goldstone legacy configuration, and updated Goldstone A-D pointings.

| Sensor                                   | Min Altitude (km) | Max Altitude (km) |
|--|-------------------|-------------------|
| Haystack/HUSIR 75E                       | 392               | 2166              |
| Goldstone (legacy pointing, before 2018) | 374               | 3373              |
| Goldstone 800 km pointing (2018 only)    | 696.6             | 857.2             |
| Goldstone Pointing A (2020-2023)         | 660.3             | 806.4             |
| Goldstone Pointing B (2020-2023)         | 709.7             | 881.0             |
| Goldstone Pointing C (2020-2023)         | 770.4             | 976.1             |
| Goldstone Pointing D (2020-2023)         | 847.5             | 1102.8            |

The fundamental measurements made by the radar are range, range-rate (or Doppler velocity), and received power from which RCS can be calculated. When operating in beampark mode, an object’s path through the beam is short; thus, obtaining full orbital information with sufficient accuracy to construct precise orbits is not possible. Using a circular orbit assumption, an object’s range and range-rate measurements can be converted to orbit altitude and Doppler inclination. This allows for analysis of detections for different orbital regimes. In addition, the RCS of an object can be converted to a physical size using the NASA Size Estimation Model (SEM), an empirical model based on laboratory measurements of representative debris objects over many orientations and a range of frequencies [4, 5].

### 3 EVOLUTION OF THE OD ENVIRONMENT

Statistical radar measurements are typically evaluated on an annual basis, which allows for observing general trends in the environment as well as effects from specific events. Fig. 1 shows an example of the environment as measured by HUSIR 75E in 2023 in terms of orbit altitude versus average Doppler inclination; corresponding detections from Goldstone are similar. In this view, highly concentrated regions of detections correspond to different orbital families. The largest of these is the sun-synchronous orbit region, clustered around the black dashed curve representing sun-synchronous altitude inclinations for circular orbits. Several notable, historic, on-orbit fragmentation events are also highlighted by black circles, where the center of each circle represents the altitude and inclination of the parent body at the time of the event [6]. A black rectangle outlines detections associated with the Starlink satellite constellation operational orbits spanning approximately 43°–53° inclination. Starlink spacecraft also operate in orbits near 70° and 97°–98° inclination, although they do not figure prominently in this paper’s time window nor contribute significantly enough to the detection rates at those altitudes and inclinations to be noticeable as separate populations in this figure. Additional populations include the NaK cloud around 65° inclination and the unassociated cloud at approximately 82° inclination.

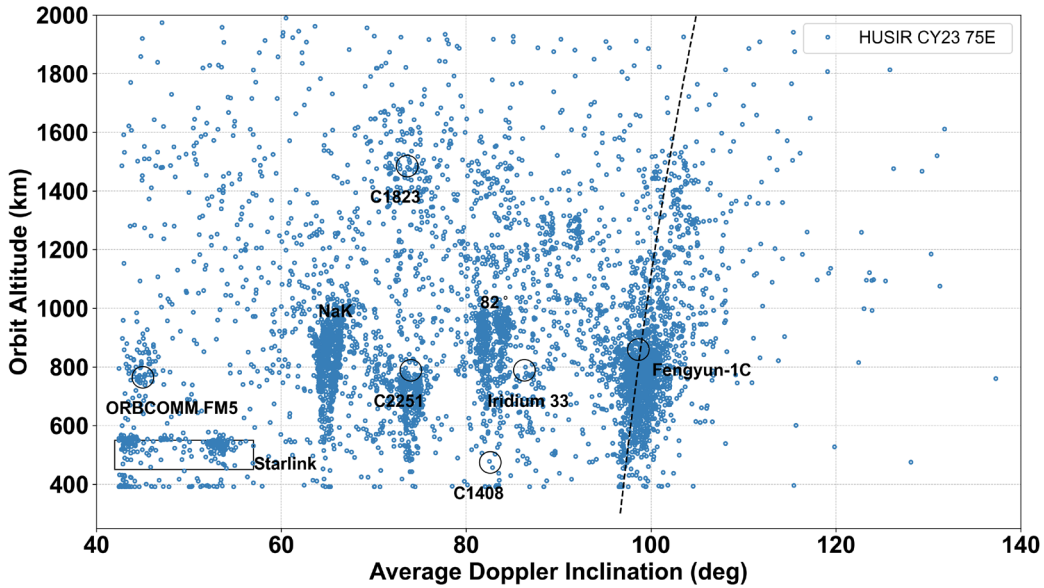


Figure 1. Orbit altitude versus average Doppler inclination for HUSIR 75E detections in CY 2023. The sun-synchronous condition, assuming a circular orbit, is indicated by the dashed black curve, and notable debris clouds and other populations are labeled.

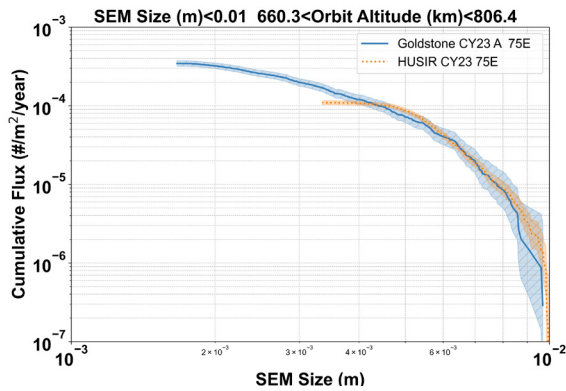


Figure 2. Cumulative flux versus SEM size for HUSIR and Goldstone in 2023, limited to sizes below 1 cm and the main beam overlap of pointing A.

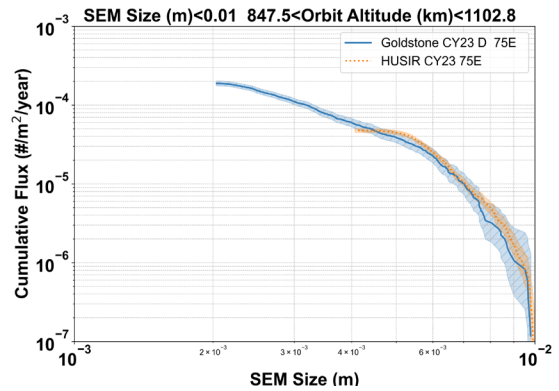


Figure 3. Cumulative flux versus SEM size for HUSIR and Goldstone in 2023, limited to sizes below 1 cm and the main beam overlap of pointing D.

Figs. 2 and 3 compare the cumulative flux versus SEM size from HUSIR and Goldstone in 2023. HUSIR's monostatic configuration covers a single range of LEO altitudes while Goldstone's bistatic pointings provide coverage of specific altitudes where the transmitter and receiver beams overlap. Because of the limited coverage for an individual pointing with this new configuration, only detections which occur in the null-to-null overlap of the transmitter and receiver beams are considered for analysis. Here, comparisons are made for specific altitude ranges corresponding to the main beam overlap of Goldstone's pointing A, 660.3 km to 806.4 km (Fig. 1),

and pointing D, 847.5 km to 1102.8 km (Fig. 2). The flux is defined as the cumulative count rate for each sensor within the specified altitude range divided by the total lateral beam surface area between the minimum and maximum altitude defining that range. The shaded regions represent the respective  $2\sigma$  Poisson uncertainty bounds. HUSIR data exhibits a roll-off in the cumulative flux below 6 mm, and Goldstone extends the size coverage from HUSIR down to approximately 2-3 mm at these altitudes. Goldstone is affected by saturation issues in the receiver at sizes around approximately 1 cm; thus, detections from both HUSIR and Goldstone have been

limited to sizes smaller than 1 cm for these comparisons. From the minimum completeness size of HUSIR to the larger roll-off size of Goldstone, the distributions from the two sensors overlap within their respective uncertainties.

In addition to capturing the current state of the OD environment, the regular measurements collected by HUSIR and Goldstone allow an assessment of the temporal evolution of the environment, though factors affecting Goldstone data availability and consistency should be noted. Maintenance downtime of the DSS-14 transmitter during 2019 and most of 2020 introduced a gap in data over 2019-2020. A single debris observation was collected using Goldstone in 2020, and the data and associated hours have been combined with the respective data collected during 2021 for better counting statistics. In addition, the decommissioning of DSS-15 and subsequent changes in the pointing configuration result in a lack of data below 650 km after 2017. Finally, relatively low numbers of Goldstone observing hours led to large uncertainties in some years, in particular 2017 and 2021. Tab. 3 provides the hours obtained and used from HUSIR 75E and Goldstone over 2016-2023, after removal of any hours identified as unusable during the data cleaning process. Goldstone hours starting in 2021 are differentiated by their specific pointing. While additional HUSIR hours are collected at the 20S and 10S pointings, data from those pointings are not included in the comparisons here so those hours are not included in Tab. 3.

Table 3. HUSIR 75E and Goldstone observation hours.

| Year | HUSIR Hours | Goldstone Hours                              |
|------|-------------|--|
| 2016 | 425.5       | 45.2   |
| 2017 | 413.5       | 13.7   |
| 2018 | 313.2       | 74.4 (800 km range)                          |
| 2019 | 116.2       | --   |
| 2020 | 120.3       | --   |
| 2021 | 146.5       | 4.2 (A)<br>10.2 (B)<br>2.7 (C)<br>12.9 (D)   |
| 2022 | 294.6       | 24.1 (A)<br>30.2 (B)<br>14.6 (C)<br>30.2 (D) |
| 2023 | 258.0       | 66.7 (A)<br>75.8 (B)<br>88.5 (C)<br>71.1 (D) |

Despite these effects, general trends in the environment can be assessed. Trends from 2016 through 2023 are shown in Figs. 4, 5, and 6 for specific altitudes of interest, including 600-650 km, 700-750 km, and 800-850 km, respectively. Due to the comparison of the different sensors and across the different Goldstone pointings, in addition to the saturation issues experienced by Goldstone for larger objects, sizes are limited to between 6 mm and 1 cm. The error bars represent the respective  $2\sigma$  Poisson uncertainty bounds. When data is available from both sensors, the fluxes at these altitudes generally agree within their respective uncertainties. Goldstone uncertainties are particularly large in some cases due to the smaller number of hours and lower number of detections as compared to HUSIR, but the HUSIR data still tends to fall within the Goldstone uncertainties in most cases.

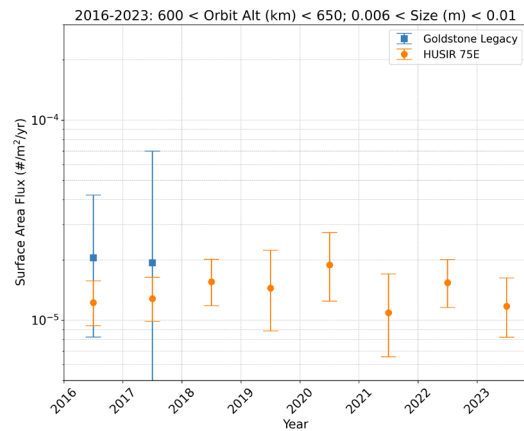


Figure 4. Surface area flux versus time for HUSIR and Goldstone from 2016-2023, limited to sizes between 6 mm and 1 cm and 600-650 km altitude.

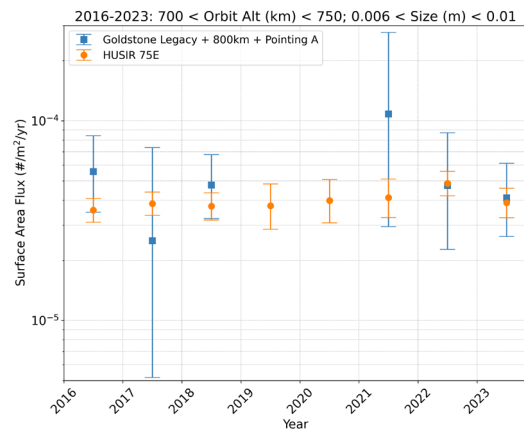


Figure 5. Surface area flux versus time for HUSIR and Goldstone from 2016-2023, limited to sizes between 6 mm and 1 cm and 700-750 km altitude.

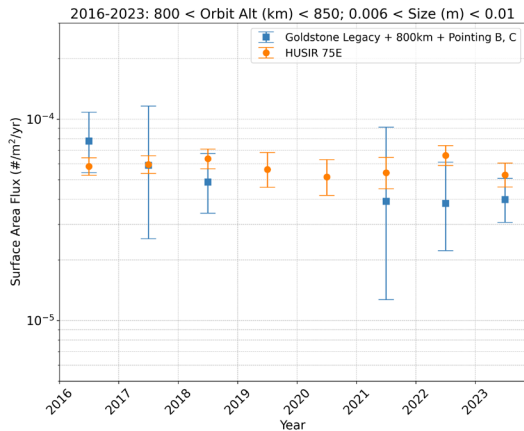


Figure 6. Surface area flux versus time for HUSIR and Goldstone from 2016-2023, limited to sizes between 6 mm and 1 cm and 800-850 km altitude.

For all altitude bands considered, the fluxes show year-to-year variability as debris decays into these altitudes from above as well as out of these altitudes to lower altitudes under the influence of atmospheric drag. The fluxes over 600-650 km altitude are consistent between Goldstone and HUSIR within their respective uncertainties in 2016 and 2017 and show fluctuations about a relatively stable average for all years considered here. Over 700-750 km altitudes, the HUSIR data also suggests variation about a relatively consistent average with a slight increase in 2022. The Goldstone data has large uncertainties in some years due to a low number of observing hours, but these uncertainties still overlap those for HUSIR. The fluxes from the two sensors in 2022 and 2023 indicate excellent agreement over this altitude band. For the 800-850 km altitude band, the Goldstone and HUSIR fluxes agree well for most years, with excellent agreement in 2017 (though with notably large uncertainties) and overlapping uncertainties in 2022.

Table 4. Significant fragmentation debris-producing events reviewed in this paper. Breakup debris statistics are taken from the SSN catalog as of 3 January 2025.

| Satellite Name | International Designator | SSN Number | Launch Date | Breakup Date | Breakup Debris    |          | Parent Body |              |                   | Breakup Type |
|----------------|--------------------------|------------|-------------|--------------|-------------------|----------|-------------|--------------|-------------------|--------------|
|                |                          |            |             |              | Cataloged to Date | On Orbit | Apogee (km) | Perigee (km) | Inclination (deg) |              |
| FY-1C          | 1999-025A                | 25730      | 10-May-99   | 11-Jan-07    | 3532              | 2557     | 865         | 845          | 98.6              | Collision    |
| Cosmos 2251    | 1993-036A                | 22675      | 16-Jun-93   | 10-Feb-09    | 1715              | 811      | 800         | 775          | 74.0              | Collision    |
| Iridium 33     | 1997-051C                | 24946      | 14-Sep-97   | 10-Feb-09    | 657               | 165      | 780         | 775          | 86.4              | Collision    |
| Cosmos 1408    | 1982-092A                | 13552      | 16-Sep-82   | 15-Nov-21    | 1807              | 14       | 490         | 465          | 82.6              | Collision    |
| NOAA 16        | 2000-055A                | 26536      | 21-Sep-00   | 25-Nov-15    | 459               | 413      | 858         | 842          | 98.9              | Explosion    |
| CZ-6A R/B      | 2022-151B                | 54236      | 11-Nov-22   | 12-Nov-22    | 794               | 677      | 847         | 813          | 98.8              | Explosion    |

## 4 SIGNIFICANT DEBRIS-GENERATING EVENTS

Several major on-orbit collisions and explosions have contributed and, in some cases, continue to contribute to the on-orbit debris population. Three major collision events and two prominent explosions are considered here; these are listed in Tab. 4.

### 4.1 Major Collisions

The first of the major collisions considered here occurred on 11 January 2007 when the FY-1C meteorological spacecraft was destroyed in an ASAT test conducted by China. The resulting debris cloud, measured by the number of trackable fragments, was and continues to be the largest in the history of spaceflight due to the long orbital lifetimes of fragments generated at the altitude of the event: 72% of the cataloged fragments remain on orbit as of 3 January 2025. Soon after the FY-1C breakup, the Haystack radar (now HUSIR) was used to collect special observations of the fragment cloud at three separate times on 22 February, 28 March, and 3 April 2007 [7], and this data was subsequently reassessed during the development of ORDEM 3.1 [8].

Fig. 7 shows the initial flux versus altitude distribution from these special data collects as compared to HUSIR CY16 and CY23 75E data over the FY-1C breakup cloud inclination band of 94°-105° for objects 6 mm and larger. The highest flux of objects larger than 6 mm from the special FY-1C observations occurs over 800-900 km altitude. While the flux from the special data collects has decreased over 800-900 km altitude by 2016 and 2023, it is similar to the background observations in 2016 and 2023 over 750-800 km altitude and just slightly lower than the flux in 2016 and 2023 over 700-750 km altitude.

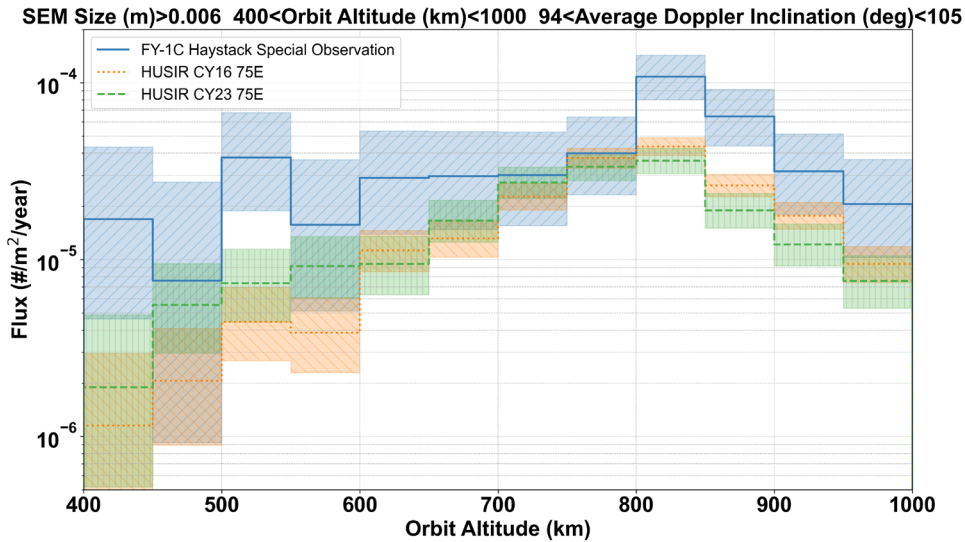


Figure 7 Surface area flux versus altitude for the FY-1C special Haystack observations, HUSIR CY16 75E, and HUSIR CY23 75E over the inclination band corresponding to the FY-1C breakup cloud, limited to sizes greater than 6 mm.

Additionally, there is evidence of a small increase from 2016 to 2023 over 700-750 km, which could be due in part to fragments from higher altitudes decaying to this altitude range over time. These comparisons indicate that this breakup cloud is still a major contribution to small debris at these altitudes, even 16 years after the event.

The second collision considered here is the accidental collision of C2251 and I33. On 10 February 2009, the derelict C2251 spacecraft accidentally collided with the operational I33 spacecraft, marking the first known accidental collision of an inoperable spacecraft with a functional spacecraft. Until the ASAT test against the C1408 spacecraft (discussed below), the C2251 and I33

fragment clouds were the second and fourth largest historical breakup clouds based on number of cataloged fragments [6]. C2251 was an older satellite while I33 was relatively modern, constructed extensively of lightweight composite materials. As a result of the differences in construction, the behavior of the two breakup clouds from this event show differences as well, with proportionally fewer fragments from the I33 breakup cloud on orbit as of 3 January 2025 as compared to the C2251 breakup cloud. Figs. 8 and 9 show the surface area flux versus altitude over the I33 and C2251 inclination bands, respectively, for the special Haystack observations of the I33/C2251 breakup cloud compared to HUSIR CY16 and CY23 75E observations limited to detections 6 mm and larger.

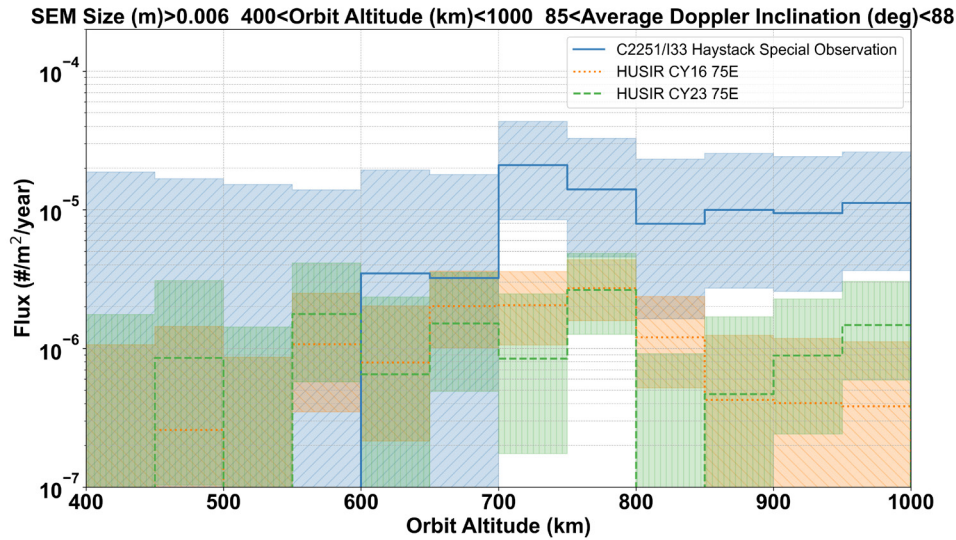


Figure 8. Surface area flux versus altitude for the I33/C2251 special HUSIR observations, HUSIR CY16 75E, and HUSIR CY23 75E over the inclination band corresponding to the I33 breakup cloud, limited to sizes greater than 6 mm.

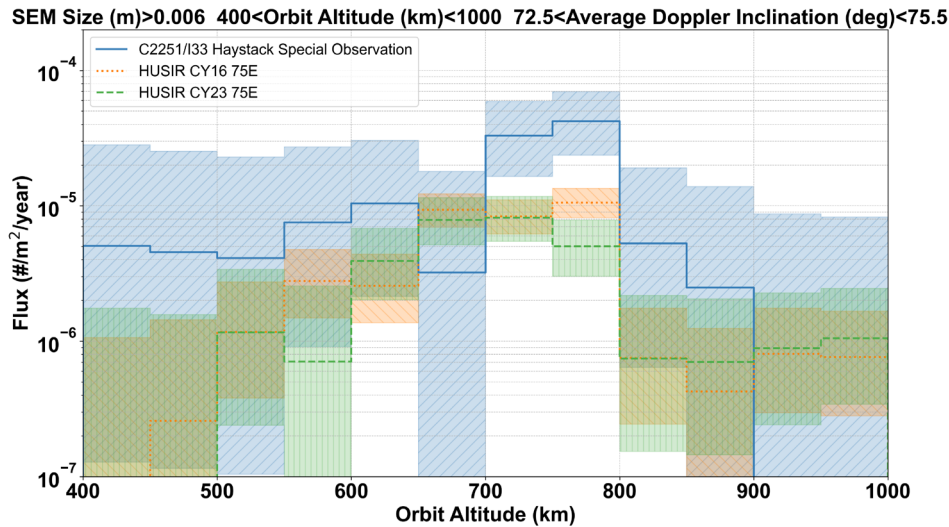


Figure 9. Surface area flux versus altitude for the I33/C2251 special HUSIR observations, HUSIR CY16 75E, and HUSIR CY23 75E over the inclination band corresponding to the C2251 breakup cloud, limited to sizes greater than 6 mm.

For the I33 inclination band of 85°-88° shown in Fig. 8, the special Haystack observations show a peak in the flux over 700-750 km altitude, and a relatively uniform flux over higher altitudes with more minor contributions from 600-700 km. By 2016, the flux is an order of magnitude below that from the special observations over 700-750 km altitude, and as of 2023, the distribution of flux over 800 km and below is relatively broad with no clear indication of a significant contribution from the original

breakup cloud. In contrast, for the C2251 inclination band of 72.5°-75.5° in Fig. 9, the initial flux shows a more distinct peak over 700-800 km altitude, with a relatively sharp decrease above 800 km and a more gradual decrease to a relatively uniform distribution across lower altitudes. By 2016, the flux over 700-800 km altitude is lower than the special observations by about a factor of 4. By 2023, the flux over 750-800 km has decreased even further to almost an order of magnitude lower than the special

observations. Conversely, the flux over 650-700 km altitude is higher than the special observations by approximately a factor of 3 in 2016 and 2023, likely due to debris decaying from higher altitudes. In general, the flux over the C2251 inclination band is more persistent than in the I33 inclination band. This is likely due to the different construction techniques and the more lightweight materials from the I33 breakup cloud decaying out of orbit faster than those for the C2251 breakup cloud.

The final collision event considered here is that of the C1408 ASAT test performed by the Russian Federation on 15 November 2021. Soon after the event, the ODPO partnered with MIT/LL, JPL, and the Space Force to collect special measurements on small C1408 debris, which matched very well to modeled predictions [9]. As a result, a rapid update to ORDEM was made to incorporate modeled fragments from the breakup, with ORDEM 3.2 released only a few months after the event [10]. The C1408 breakup is now the second largest historical breakup cloud based on number of cataloged fragments, with 1807 fragments cataloged as of 3 January 2025; however, only 27 fragments remain on orbit as of the same epoch.

The flux as a function of altitude is shown in Fig. 10 over the C1408 inclination band of  $81^{\circ}$ - $84^{\circ}$  and to a limiting size of 6 mm, comparing the C1408 special HUSIR observations to the background HUSIR measurements in 2021, 2022, and 2023. Because the breakup occurred late

in 2021, it was not evident in the regular background observations of 2021, and 2022 was the first year the debris from this breakup was apparent in the statistical observations. The effect of this breakup on altitudes below 600 km is apparent, with the 2021 flux at nearly non-existent levels and the special observations reaching a significant peak over 400-550 km altitude. By 2022, the flux drops by at least 2 orders of magnitude over 400-550 km altitude. As of 2023 the flux below 500 km is nearing pre-breakup levels, with the flux from 500-550 km relatively stable from 2022 to 2023.

A similar result is seen when viewing the evolution of the flux over time as in Fig. 11 for the C1408 inclination band and 400-600 km altitude. The flux over this altitude range is very consistent from 2016 through 2020, with an apparent drop in 2021. There is a significant spike of approximately 3 orders of magnitude over the background levels seen in the HUSIR special observations and a maintained increase of approximately an order of magnitude over 2016-2020 levels seen in the year after the breakup; however, as of 2023, the flux is again comparable to background levels. The relatively low altitude of the breakup in combination with increased solar flux activity have caused this breakup cloud to decay faster than originally anticipated based on modeling assessments [11].

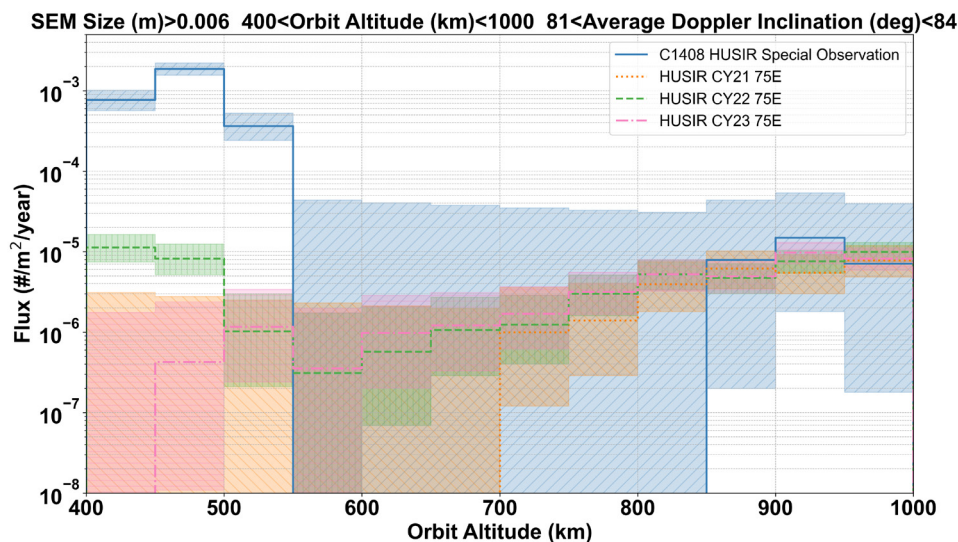


Figure 10. Surface area flux versus altitude for the C1408 special HUSIR observations compared to background HUSIR observations from 2021-2023 over the inclination band corresponding to the C1408 breakup cloud, limited to sizes greater than 6 mm.

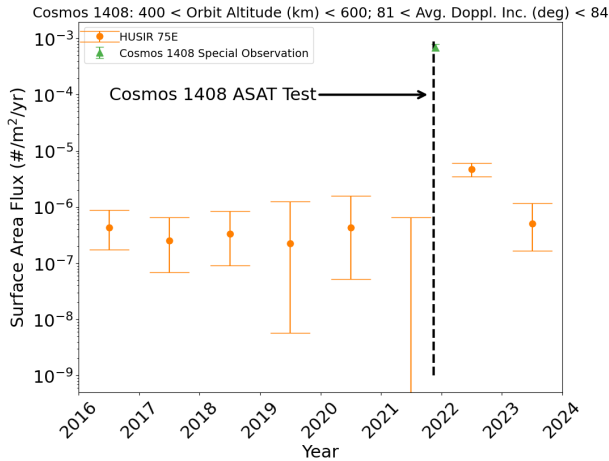


Figure 11. Surface area flux versus time for HUSIR from 2016-2023 over the inclination band corresponding to the Cosmos 1408 breakup cloud and 400-600 km altitude, limited to sizes 6 mm and larger.

#### 4.2 Prominent Explosions

In November 2015, the decommissioned NOAA-16 weather satellite experienced a major breakup event, assessed to likely be a battery-related explosion. In terms of number of fragments cataloged, the NOAA-16 breakup is the third worst breakup event of a payload not caused by a collision (*i.e.*, due to an explosion or an unknown cause), and the worst payload explosion in terms of the number of fragments remaining on orbit. Of the major breakups considered here, NOAA-16 has the highest percentage of fragments still remaining on orbit at nearly 90% as of 3 January 2025.

Nearly 7 years after the NOAA-16 explosion, in November 2022, a CZ-6A upper stage associated with China’s Yunhai-3 weather satellite exploded just one day after its launch, in an orbit similar to that of the NOAA-16 spacecraft. The CZ-6A explosion is currently the worst breakup event of an upper stage in terms of number of cataloged fragments, and fourth worst event overall. In terms of number of fragments remaining on orbit, it is currently the third worst breakup event.

The similar orbits of NOAA-16, CZ-6A, and FY-1C at their respective times of breakup introduce challenges to being able to distinguish between the effects of the breakup events over long periods of time, especially given the significantly higher number of fragments from the FY-1C breakup and the long lifetimes of fragments at these altitudes. Models of the NOAA-16 and CZ-6A breakups, as well as orbit distributions of cataloged fragments, indicate fragments from those breakup clouds cover inclinations in the range 98°-100°, a much narrower inclination band than that

exhibited by the special FY-1C data collects and cataloged FY-1C fragments. Comparing the evolution of the flux over time for these inclination bands can provide insight into the relative contribution of fragments from these different events. Fig. 12 shows the flux from 2016-2023 over the wider FY-1C inclination band (94°-105°) and the narrower NOAA-16/CZ-6A inclination band (98°-100°) over 700-750 km altitude. This altitude range covers the orbits of the NASA “A-Train” spacecraft. Similarly, Fig. 13 shows the fluxes from 2016-2023 over 650-700 km altitude, where two of the original A-train spacecraft – Aqua and Aura – now reside as they have slowly drifted out of the original A-train altitude band. While the uncertainties in the fluxes overlap for many of the years, over 700-750 km altitude, the flux is relatively stable from 2016-2020 for both inclination bands, with evidence of an increasing trend from 2020 to 2023. For 650-700 km altitudes, there is a more distinct increase in fluxes over the FY-1C inclination band from 2016 to 2019, followed by an additional increase from 2020 to 2023. In nearly all years, the contribution from the NOAA-16/CZ-6A inclination band is at least half of the flux from the FY-1C inclination band. For 650-700 km altitudes, this relative contribution is even more significant in the later years, likely due to fragments from the NOAA-16 breakup decaying from higher altitudes into this altitude range, as also seen by the behavior of cataloged fragments in the previous analyses of [12]. This is likely due to an increase in solar activity over these years from the start of solar cycle 25. Due to the timing of the CZ-6A breakup late in 2022, its contribution likely will not reach full effect until the coming years, and its influence will be monitored with the regular radar data collects.

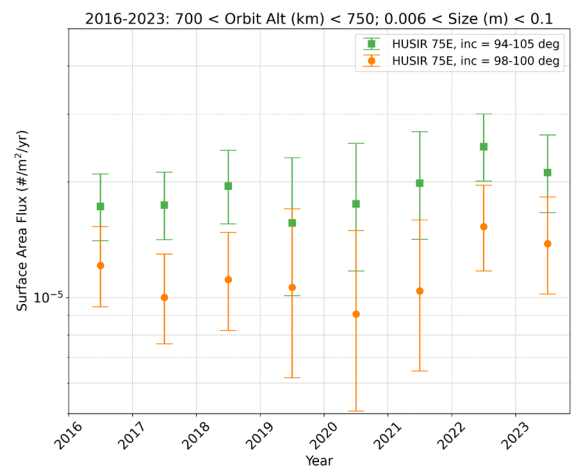


Figure 12. Surface area flux versus time for the background HUSIR observations from 2016-2023 over 700-750 km altitude, the inclination bands corresponding to the FY-1C breakup cloud (94°-105°) and NOAA-16/CZ-6A breakup clouds (98°-100°), and sizes between 6 mm and 10 cm.

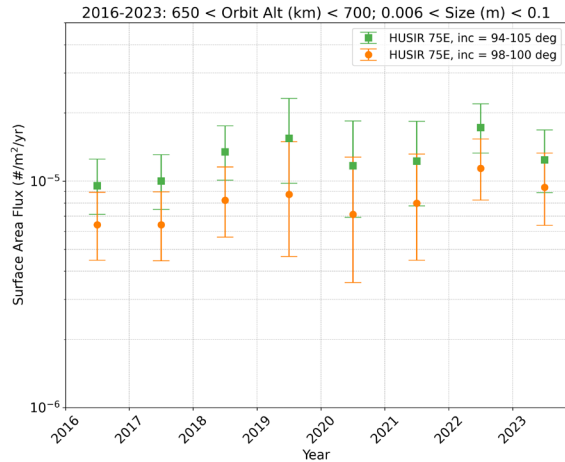


Figure 13. Surface area flux versus time for the background HUSIR observations from 2016-2023 over 650-700 km altitude, the inclination bands corresponding to the FY-1C breakup cloud (94°-105°) and NOAA-16/CZ-6A breakup clouds (98°-100°), and sizes between 6 mm and 10 cm.

### 4.3 NaK

The NaK population was originally identified in the early 1990s in Goldstone and Haystack radar data. It represented a population of electrically conducting spheres from a few millimeters to a few centimeters in size, all in 65° inclination, near-circular orbits, mostly between the altitudes of 850 and 1000 km. The spherical nature was deduced from the strong PP and very weak OP returns, and MIT/LL was able to catalog a few of the objects, determine their ballistic coefficients, and measure their optical properties [13]. The evidence pointed to electrically conducting spheres with densities consistent with the NaK liquid metal coolant used in the Soviet Radar Ocean Reconnaissance Satellite (RORSAT) reactors, which had nuclear cores jettisoned into these orbits in the 1980s. In the microgravity of orbit, the droplets formed into individual spheres. Radar observations indicate that NaK spheres may also be produced by phenomena distinct from core separation. In addition to the RORSAT sources, “Topaz” reactors (aboard Cosmos 1818 and 1867) have also been noted to produce NaK droplets in their operational orbits, though they did not separate reactor cores [14].

Based on analysis of detections with polarizations close to 1 and inclinations near 65°, a filter has been developed to extract those detections most likely to be NaK from the HUSIR data. For the years considered here, detections from the 75E pointing are deemed to be NaK if they have an altitude less than 1000 km; average Doppler inclination

between 62.9° and 67°; and polarization greater than a limit derived from inspection of data – a piecewise linear function of PP RCS [14]. A similar filter has been developed for the 20S and 10S pointings, but those configurations have more limited data available for analysis.

Fig. 14 shows the time evolution of the NaK population as detected by HUSIR 75E over 2016-2023. Over these years, the NaK population exhibits a slight decrease from 2018 to 2019, with a markedly stable flux thereafter. The cumulative count rate as a function of the PP RCS for 2016, 2018, 2020, and 2023, as well as the composite count rate over 2016-2023, is shown in Fig. 15. The RCS distribution for NaK is expected to show an inflection point near -35 dBsm based on empirical models [14, 15]. The HUSIR data exhibits the expected rapid increase in count rate near -35 dBsm, with a small shift from the expected value likely due to calibration and data processing effects. As with the flux over time, the curves show similar behavior over multiple years, with a slight decrease in the distribution below approximately -40 dBsm from 2016 to 2023. These results are consistent with the findings in [14], suggesting a relatively stable population, and point to possible ongoing production from higher altitudes that is replenishing objects at lower altitudes as they decay.

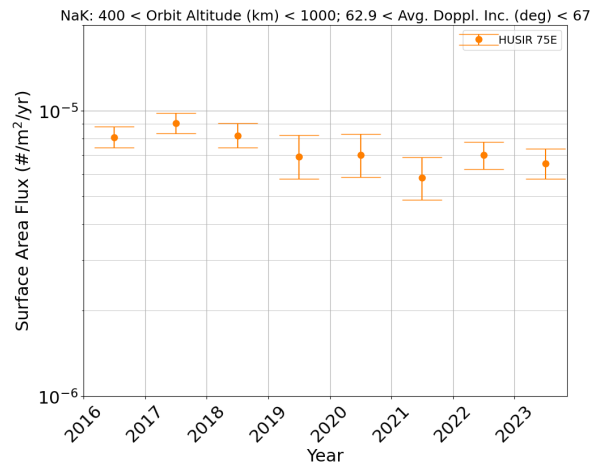


Figure 14. Surface area flux versus time for the NaK population from HUSIR 75E over 2016-2023, with sizes limited to 6 mm.

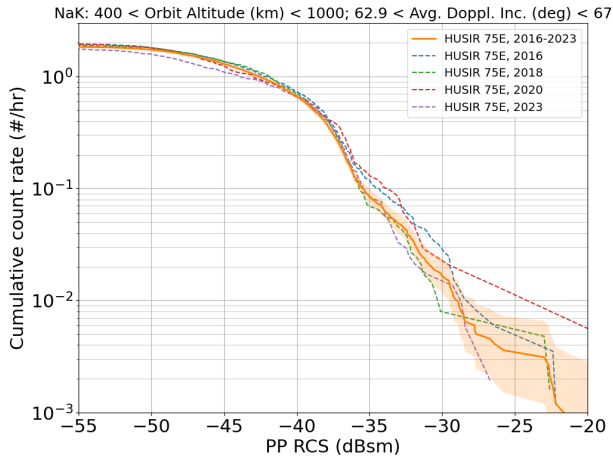


Figure 15. Cumulative count rate versus PP RCS for HUSIR NaK detections as a composite over 2016-2023 and yearly snapshots from 2016, 2018, 2020, and 2023.

#### 4.4 82° Cloud

As with the NaK population, a persistent anomalous debris cloud has been identified through analysis of HUSIR data. This cloud is apparent at an inclination of approximately 82° and below 1200 km in altitude (see Fig. 1). Several candidate sources have been investigated, and while no parent body or source mechanism has yet been identified, observations suggest this cloud is consistent with one or more low debris mass, low velocity, non-energetic events [16].

Fig. 16 shows the surface area flux as a function of time for HUSIR detections over the inclination band corresponding to the 82° cloud. While the fluxes are consistently within a factor of 2 from 2016 to 2023, there is evidence of a slight increase over time. The cumulative count rate as a function of size for this population in 2016, 2018, 2020, and 2023, and the composite count rate over 2016-2023, is shown in Fig. 17. These distributions also indicate an increase in the count rates of sub-centimeter objects since 2016, supporting the hypothesis of an ongoing low-velocity production mechanism. This population will continue to be monitored by regular radar observations, and analysis will continue to better identify potential production sources and inform necessary adjustments to models of the small debris population.

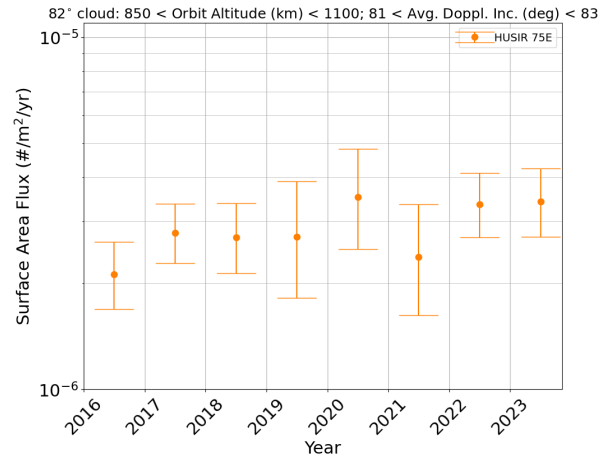


Figure 16. Surface area flux versus time for HUSIR from 2016-2023 over the inclination band corresponding to the 82° cloud, with sizes limited to 6 mm and larger.

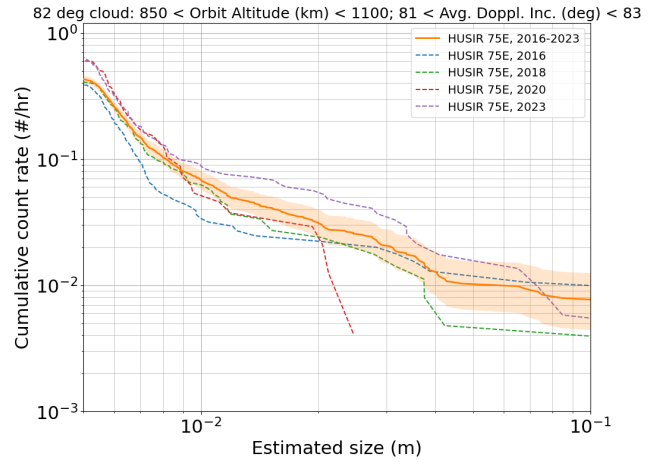


Figure 17. Cumulative count rate versus size for HUSIR detections from the altitude and inclination region corresponding to the 82° cloud as a composite over 2016-2023 and yearly snapshots from 2016, 2018, 2020, and 2023.

## 5 CONCLUSION

Long-term observations of the OD environment, such as those conducted with HUSIR and Goldstone, enable longitudinal studies of the growth of the total environment (and hence, risk to crewed and robotic vehicles) as well as the evolution of individual fragmentation debris clouds and other sources of small debris.

Significant findings presented in this paper are that:

- 1) The FY-1C breakup continues to contribute to the flux of debris less than 1 cm, particularly from 700-800 km altitude.
- 2) Fragments from the C2251 fragments still contribute non-negligibly around 700 km altitude, while the I33 fragments no longer have a significant influence on the fluxes within the I33 inclination band.
- 3) The C1408 breakup cloud has mostly disappeared from the radar data as of 2023 observations.
- 4) There is evidence of an increasing influence from decaying NOAA-16 breakup fragments over 650-750 km altitude.
- 5) The NaK population appears to be relatively stable.
- 6) The 82° cloud has increased within a factor of 2 from 2016 to 2023, suggesting an ongoing production mechanism.

Continued regular observations from both HUSIR and Goldstone will offer insight on the behavior of known events and provide the data necessary to investigate and identify currently unknown sources that contribute to the growth of the small debris population in LEO, informing updates to models of the OD environment.

## 6 REFERENCES

1. Murray, J. & Kennedy, T. (2022). Haystack Ultra-Wideband Satellite Imaging Radar Measurements of the Orbital Debris Environment: 2020, NASA/TP-20220006634.
2. Murray, J. & Matney, M. (2023). Haystack Ultrawideband Satellite Imaging Radar Measurements of the Orbital Debris Environment: 2021, NASA/TP-20230008344.
3. Arnold, J. A., Murray, J., Murray, M., Matney, M., & Kennedy, T. (2024). Goldstone Radar Measurements of the Orbital Debris Environment: 2020-2021, NASA/TP-20240002199.
4. Handbook for Limiting Orbital Debris, NASA-Handbook 8719.14 (2008).
5. Xu, Y.-L., Stokely, C., Matney, M., & Stansbery, E. (2005). A Statistical Size Estimation Model for Haystack and HAX Radar Detections. 56th International Astronautical Congress, Fukuoka, Japan.
6. Anz-Meador, P., Opiela, J., & Liou, J.-C. (2022). History of On-Orbit Satellite Fragmentations, 16th Edition, NASA/TP-20220019160.
7. Stansbery, E., Matney, M., Liou, J.-C., & Whitlock, D. (2008). A Comparison of Catastrophic On-Orbit Collisions. Proceedings of the Advanced Maui Optical and Space Surveillance Technologies Conference, Wailea, Maui, Hawaii, September 17-19, 2008.
8. Manis, A., Matney, M., Vavrin, A., Seago, J., Gates, D., Anz-Meador, P., Kennedy, T., Cowardin, C., Xu, & Yu-Lin (2022). NASA Orbital Debris Engineering Model (ORDEM) 3.1: Model Process, NASA/TP-20220004345.
9. NASA ODPO (2022). The Intentional Destruction of Cosmos 1408, *Orbital Debris Quarterly News* 26(1), pp. 1-5 <https://orbitaldebris.jsc.nasa.gov/quarterly-news/pdfs/ODQNV26i1.pdf> [Retrieved 16 Dec 2024].
10. NASA ODPO (2022). Orbital Debris Engineering Model 3.2 Release, *Orbital Debris Quarterly News* 26(1), p. 5 <https://orbitaldebris.jsc.nasa.gov/quarterly-news/pdfs/ODQNV26i1.pdf> [Retrieved 24 Feb 2025].
11. Manis, A., Matney, M., & Anz-Meador, P. (2024). Evolution of the Cosmos 1408 Breakup Cloud: A Two-Year Status, *Orbital Debris Quarterly News* 28(2), pp. 2-4 <https://orbitaldebris.jsc.nasa.gov/quarterly-news/pdfs/ODQNV28i2.pdf> [Retrieved 16 Dec 2024].
12. Anz-Meador, P., King, A., & Matney, M. (2023). Evolution of Major Debris Clouds in Low Earth Orbit, *Orbital Debris Quarterly News* 27(3), pp. 7-11 <https://orbitaldebris.jsc.nasa.gov/quarterly-news/pdfs/ODQNV27i3.pdf> [Retrieved 13 Dec 2024].
13. R. Sidharan, Beavers, W., Lambour, R., Gaposchkin, E.M., Kansky, J., & Stansbery, E. (1977). Remote Sensing and Characterization of Anomalous Debris, In Proceedings of Second European Conference on Space Debris, Darmstadt (ESA SP-393, May 1997).
14. Matney, M., Anz-Meador, P., Murray, J., Miller, R., & Kennedy, T. (2019). The NaK Population: a 2019 Status. First International Orbital Debris Conference, Houston, TX, 9-12 December 2019.
15. Foster, J.L., Krisko, P., Matney, M., & Stansbery, G. (2003). NaK Droplet Source Modeling. IAC-03-IAA.5.2.02.
16. Gates, D. & Anz-Meador, P. (2019). An 82° Inclination Debris Cloud Revealed by Radar.

First International Orbital Debris Conference,  
Houston, TX, 9-12 December 2019.